Mature dentate granule cells show different intrinsic properties depending on the behavioural context of their activation

Angélique Peret[1+], Claire Pléau[1+], Edouard Pearlstein[1], Thomas Scalfati[1], Geoffrey Marti[2], François Michel[1] and Valérie Crépel[1#]

[1]INMED, INSERM UMR1249, Aix-Marseille Université, Marseille, France.

[2]ISM, Aix-Marseille Université, CNRS, Marseille, France.

[+] These authors contributed equally to this work

corresponding author: valerie.crepel@inserm.fr

Figures: 5

Table: 1

Supplemental Materials: 2 figures and 1 table

Abstract

The dentate gyrus (DG) plays a crucial role in learning, memory and spatial navigation. Only a small fraction of mature dentate granule cells (mDGCs) is active during behaviour, while the large majority remains silent. To date, the properties of this active subset of neurons remains poorly investigated. Using fosGFP transgenic mice, we show *ex vivo* that activated mDGCs, from mice in their home cage, exhibit a striking lower intrinsic excitability associated with a shorter axon initial segment when compared to the non-activated cells. Remarkably, activated mDGCs, from mice trained in a virtual environment, are more excitable than those in the home cage condition. Therefore, we show that activated mDGCs display different intrinsic properties and excitable states depending on the behavioural contexts of their activation. We propose that these properties could constitute the neural signature of cell assemblies involved in specific behavioural contexts such as a familiar environment or spatial training.

Introduction

The dentate gyrus (DG), an input region of the hippocampal formation, plays a crucial role in learning, memory and spatial navigation (McNaughton and Morris, 1987). Memory storage and recall involve a discrete population of cells within the DG region (Tonegawa et al., 2015). Only a small fraction of dentate granule cells (DGCs) is active during behaviour, while the large majority remains silent (Chawla et al., 2005; Diamantaki et al., 2016; Jung and McNaughton, 1993; Neunuebel and Knierim, 2012; Pilz et al., 2016; Skaggs et al., 1996; Stefanelli et al., 2016; Tonegawa et al., 2015). Since the discovery of the DG's ability to generate new neurons throughout life (Aimone et al., 2011), it has been proposed that DG neurogenesis provides a substrate for spatial memory and pattern separation (Aimone et al., 2011; Clelland et al., 2009; Kropff et al., 2015; Leutgeb et al., 2007; McNaughton and Morris, 1987; Nakashiba et al., 2012; Neunuebel and Knierim, 2014; Sahay et al., 2011). This role would be facilitated by the high excitability of newly generated neurons (Aimone et al., 2011; Cameron and Mckay, 2001; Kempermann et al., 1997; Lopez-Rojas and Kreutz, 2016; Ninkovic et al., 2007). On the other hand, recent studies have shown that mature dentate granule cells (mDGCs) play a major role in pattern completion (Nakashiba et al., 2012) and are required for recall of familiar contexts (Vukovic et al., 2013). However, at present the intrinsic physiological properties of these mature cells remain poorly investigated in contrast to those of adult born DGCs. Notably it is yet unestablished whether mDGCs display uniform intrinsic properties or whether these properties could vary depending on the behavioural context of their activation.

Here, we examined *ex vivo* the intrinsic electrophysiological properties of activated DGCs from mice maintained in their home cage or trained in a virtual reality (VR) environment compared to the non-activated cells. The analysis of intrinsic properties of DGCs activated in these conditions was performed using a fluorescent cellular tagging approach based on a

transgenic mouse model in which the expression of the enhanced green fluorescent protein (EGFP) is controlled by the promoter of the activity-dependent gene *c-fos* (Barth et al., 2004; Czajkowski et al., 2014). Accordingly, activated neurons during a given behavioural task will express shortly and transiently the fluorescent protein allowing for their identification for electrophysiological analysis on acute brain slices (Barth et al., 2004). Our data reveal that activated mDGCs, from mice in their familiar home cage, exhibit different intrinsic properties and a striking lower excitability when compared to the non-activated cells. This is associated with a modification of the action potential waveform and a shorter axon initial segment. Remarkably, activated mDGCs from mice trained in virtual environment display a more excitable state when compared to the home cage condition. This is dependent on the presence of visual cues during the training period. Therefore, our study shows that mDGCs do not constitute a uniform cell population since they display diverse intrinsic properties depending on the behavioural context of their activation. We propose that these properties could constitute the electrophysiological signature of different cell assemblies involved in specific contexts such as a familiar environment or spatial training.

Results

fosGFP^{+} cells display characteristics of mature DGCs in home cage condition and in trained mice

In a first set of experiments, we examined the fraction of DGCs activated in different behavioural contexts. We studied the percentage of DGCs activated in the home cage condition and during training in a virtual linear track. For the training in a virtual linear track, the task was performed using a virtual reality (VR) system (Dombeck et al., 2010; Harvey et al., 2009; Ravassard et al., 2013) (see Materials and Methods). The VR, which creates the perception of reality in a simulated environment, offers unique advantage for studying the

specific role of visual cues in learning of spatial navigation (Dombeck et al., 2010; Harvey et al., 2009; Hölscher et al., 2005; Youngstrom and Strowbridge, 2012). Head-restrained mice were trained to run back and forth along a 150 cm-long bidirectional virtual linear track that had proximal and distal walls with varying patterns as visual cues for orientation (Figure 1A, B). The mouse, which was water restricted throughout the experiment (see Materials and Methods), received a water reward at the end of the track after successfully traversing the full track length. After receiving a reward at the first reward zone, the mouse then had to run to the other end of the track to receive the next reward. In the first sessions (up to 8), the mice moved slowly and erratically along the track as they learned the task. By 8-10 sessions, the mice moved consistently back and forth along the track, and they received rewards at increasing rates over time (1.14 ± 0.05 reward/min, n = 9 mice) consistent with learning of the task (Figure 1C). We also observed that mice reliably slowed down before reaching the track end suggesting that they learned to anticipate the location of the reward zones (Figure 1C). To test the role of visual cues on behaviour, mice were trained with the same VR system (see Materials and Methods) but without visual cues (hereafter referred to as training without visual cues) (Figure 1C, D) (Youngstrom and Strowbridge, 2012). Mice trained in this condition also learned to move along the track as shown by a progressive increase in the number of rewards per session (Figure 1C). After 8-10 sessions, mice moved consistently back and forth along the track and we did not observe a significant difference of reward frequency compared with mice trained with visual cues (Figure 1C). Furthermore, without visual cues, mice ran with a similar average speed than mice trained with visual cues (10.2 ± 0.18 cm/s with visual cues, n = 8 mice; 10.5 ± 0.05 cm/s without visual cues, n = 8 mice, p=0.941). However, without visual cues mice ran with a uniform speed compared with the mice trained with visual cues and they did not anticipate the reward zone since they did not slow down their speed before reaching the track end (Figure 1C). Altogether, these results

showed that visual cues played a major role for mice to adapt their running performance between water reward locations on a linear virtual track as previously described (Youngstrom and Strowbridge, 2012).

To analyse the fraction of DGCs activated in the different behavioural contexts (see above), we used a strain of transgenic mice in which the expression of EGFP is controlled by the promoter of the activity-dependent immediate early gene (IEG) *c-fos* (see Materials and Methods). These mice enabled an *ex vivo* characterization of cells a few hours after their activation (Barth et al., 2004). In training conditions with or without visual cues, examination of cells expressing fosGFP was performed *ex vivo* in hippocampal slices obtained shortly after the last training session (about 20-25 sessions, see Materials and Methods). Quantification of cells expressing fosGFP was performed in the septal pole of the hippocampus, which is known to play a crucial role in spatial memory (Moser et al., 1993). When mice (water restricted) were maintained in their home cage, a small fraction (1.06 ± 0.1% of DGCs, n = 25 slices, n = 6 mice) of cells expressed fosGFP as shown by immunohistochemistry using EGFP antibody (see Materials and Methods) (Figure 1D, E). By contrast, mice trained with visual cues (see above and Materials and Methods) displayed a significant higher fraction of $fosGFP^+$ cells in the septal hippocampus (1.92 ± 0.16% of DGCs, n = 19 slices, n = 5 mice, $p < 0.0001$) (Figure 1D, E). When mice were trained without visual cues, we did not observe a significant difference in the fraction of $fosGFP^+$ cells in the septal hippocampus (0.9 ± 0.18% of DGCs, n = 13 slices, n= 4 mice, p=0.408) compared to the home cage condition (Figure 1E). Therefore, the data show that, in our training conditions, the increase in the number of $fosGFP^+$ cells in the septal hippocampus requires visual cues.

We then explored the distribution of $fosGFP^+$ cells across the DG in septal hippocampus in the different experimental conditions. To address this question, we plotted the localization of $fosGFP^+$ cells in DG and investigated their lateral and radial distributions. DG cell layer

extends laterally from the upper (suprapyramidal) blade to the lower (infrapyramidal) blade and from the outer layer (near the molecular layer) to the inner layer (near the hilus) in a radial direction (Altman and Bayer, 1990). In order to reliably quantify the position across data we used normalized coordinates (see Materials and Methods). We plotted the distribution and the count of fosGFP$^+$ cells (Figure 2A, B). Our data showed that for all experimental conditions, a majority of fosGFP$^+$ cells were located in the upper blade of dentate granule cell layer (67 ± 4.7%, n = 25 slices, n = 6 mice in home cage condition; 62 ± 3.2%, n = 19 slices, n = 5 mice trained with visual cues; 72 ± 4.7%, n = 13 slices, n = 4 mice trained without visual cues) and close to the molecular layer (74 ± 2.9%, n = 25 slices, n = 6 mice in home cage condition; 67 ± 2%, n = 19 slices, n = 5 mice trained with visual cues; 72 ± 4%, n = 13 slices, n = 4 mice trained without visual cues) (Figure 2A, B). Furthermore, immunohistochemistry performed with Prox1 antibody confirmed that most fosGFP$^+$ cells corresponded to DGCs; we found that more than 95% of these neurons were co-labelled with EGFP and Prox1 antibodies (97.2%, n = 36 cells, n = 3 mice in home cage condition; 98.5%, n = 130 cells, n = 5 mice trained with visual cues; 100%, n = 31 cells, n = 2 mice trained without visual cues) (Figure 2C, figure supplement 1B). Altogether, this strongly suggested that fosGFP$^+$ cells corresponded to mDGCs and not to adult-born cells, since adult-born neurons are preferentially located close to the hilus (Zhao et al., 2008). To identify adult-born DGCs, we used an anti–doublecortin (DCX) antibody, a specific marker of newly born neurons (Zhao et al., 2008). We did not find any fosGFP$^+$ DGC co-labelled with DCX antibodies (Figure 2C, figure supplement 1C) in the home cage condition and in mice trained with or without visual cues, confirming that fosGFP$^+$ cells did not correspond to adult-born neurons in our experimental conditions.

Overall, our data reveal that fosGFP$^+$ DGCs activated in home cage condition or during training corresponded to mDGCs. Furthermore, we observe that training with visual cues

induces an increase in the number of fosGFP$^+$ DGCs compared to the home cage condition and training without visual cues.

fosGFP$^+$ DGCs display a low intrinsic excitability in mice in home cage

The firing pattern of fosGFP$^+$ and fosGFP$^-$ DGCs from mice in the home cage condition was examined *ex vivo* in slices using patch-clamp recordings (see Materials and Methods). We observed a striking lower excitability in fosGFP$^+$ DGCs compared with the fosGFP$^-$ cells as shown by the f/I plots (see Materials and Methods) with a lower gain (0.37 ± 0.04 Hz/pA and 0.12 ± 0.02 Hz/pA in 29 fosGFP$^-$ DGCs and 18 fosGFP$^+$ DGCs, respectively, $p<0.0001$) (Figure 3A, B, C) (Table). This difference in firing frequency was not associated with a modification of the action potential (AP) threshold, amplitude and half-width (Table). We then analysed the passive membrane properties of fosGFP$^-$ (n = 29 cells) and fosGFP$^+$ DGCs (n = 21 cells). We observed a lower input resistance (Rin) (343.1 ± 21.9 MΩ and 191 ± 12 MΩ in fosGFP$^-$ DGCs and fosGFP$^+$ DGCs, respectively, $p< 0.0001$) associated with a higher rheobase (35.2 ± 2.4 pA and 82.9 ± 9.8 pA in fosGFP$^-$ DGCs and fosGFP$^+$ DGCs, respectively, $p< 0.0001$) (Figure 3D, E) (Table) without a significant change in resting membrane potential (RMP) when compared to fosGFP$^-$ DGCs (Table). Moreover, we observed that the difference of Rin in fosGFP$^+$ was not dependent on AMPA and GABA-A receptors since we observed a similar Rin in the presence of NBQX (10 µM) and Gabazine (5 µM) (228.6 ± 18.6 MΩ, n = 9 fosGFP$^+$ DGCs, $p=0.098$) (not shown).

In conclusion, our data show that fosGFP$^+$ DGCs activated in the home cage condition display a lower intrinsic excitability compared to fosGFP$^-$ DGCs.

fosGFP$^+$ DGCs display a different excitable state when mice are trained with visual cues

Our histological analysis has revealed that training with visual cues induced an important increase in the number of fosGFP$^+$ DGCs (see above). In order to study the intrinsic properties of this subset of activated neurons, we examined their firing pattern and intrinsic properties *ex vivo* in slices (see Materials and Methods). In these cells, we observed a higher excitability (Figure 3A, B) and gain (0.21 ± 0.03 Hz/pA, n = 16, p=0.0076) (Figure 3C) when compared to fosGFP$^+$ cells in home cage condition (Figure 3A, B, C); this was associated with a higher input resistance (Rin) (254 ± 23 MΩ in 16 fosGFP$^+$ DGCs, p=0.0132) and a lower rheobase (43.8 ± 4.2 pA in 16 fosGFP$^+$ DGCs, p=0.0029) without a significant change neither in RMP (p=0.052), nor threshold (p=0.76), amplitude (p=0.824) or half-width (p=0.536) of AP (Table). Moreover, we observed that Rin in fosGFP$^+$ was not dependent on AMPA and GABA-A receptors since we observed a similar Rin in the presence of NBQX (10 µM) and Gabazine (5 µM) (258.5 ± 24.5 MΩ, n = 7 fosGFP$^+$ DGCs, p=0.4921) (not shown). Remarkably, these fosGFP$^+$ DGCs still remained less excitable than fosGFP$^-$ cells (Figure 3A, B, C, D) (Table). We then examined whether fosGFP$^+$ DGCs from mice trained without visual cues could display different intrinsic excitability. We observed that cells from mice trained in this condition displayed neither a significant difference in gain (p=0.573), nor input resistance (p=0.841) or rheobase (p=0.425) when compared to the home cage condition (Figure 3) (Table). This revealed that only fosGFP$^+$ DGCs trained with visual cues displayed a higher excitable state when compared to the home cage condition or training without visual cues. Finally, our data unveiled that fosGFP$^-$ DGCs constituted an homogenous population since they displayed similar excitability and intrinsic properties across all experimental conditions (Figure 3) (Table) showing that the diversity of intrinsic properties is restricted to fosGFP$^+$ DGCs.

Taken together, our data show that fosGFP$^+$ DGCs from mice trained with visual cues display a more excitable state when compared to the home cage condition or mice trained without visual cues.

fosGFP$^+$ DGCs display a different AP waveform and AIS length

Besides passive and voltage-dependent conductances, intrinsic excitability is tightly regulated by the site of spike initiation in the axon initial segment (AIS) (Araki and Otani, 1955; Bean, 2007; Bender and Trussell, 2012; Coombs et al., 1957; Debanne et al., 2011; Grubb and Burrone, 2010a; Kole and Stuart, 2012; Petersen et al., 2016; Scott et al., 2014; Wefelmeyer et al., 2016). When it is recorded at the somatic level, AP waveform generally comprises two distinct components (Colbert and Johnston, 1996; Coombs et al., 1957; Fuortes et al., 1957; Grace and Bunney, 1983; Häusser et al., 1995), the first peak reflecting the spike initiation in AIS and the second peak the somato-dendritic spike (Bean, 2007). To test a putative modification of AP initiation in AIS in our experimental conditions, we examined the AP waveform in fosGFP$^+$ and fosGFP$^-$ DGCs using phase plot analysis consisting in the second-derivative of the somatic membrane potential (d^2V/dt^2) as a function of somatic membrane potential (Figure 4A) (see Materials and Methods); the second-derivative analysis allowed a good resolution of the two components of the AP phase plot (AIS peak vs. somato-dendritic peak) (Kress et al., 2008; Meeks and Mennerick, 2007). We then evaluated the fraction of fosGFP$^-$ and fosGFP$^+$ DGCs exhibiting an AP phase plot with one or two peaks (Figure 4B); the first peak was discriminated from the second one using the analysis of the stationary inflection point (Kress et al., 2008). We showed that a majority of fosGFP$^-$ DGCs displayed a phase plot with two peaks across all experimental conditions (86%, 25 out of 29 cells in home cage condition; 88%, 23 out of 26 cells in mice trained in VR with visual cues; 88%, 7 out of 8 cells in mice trained in VR without visual cues) (Figure 4B). On the contrary, only around

half of fosGFP$^+$ displayed a phase plot with two peaks; a significant fraction (p=0.0002) of fosGFP$^+$ DGCs displayed a phase plot with a different dynamic, since the first peak could not be detected in this neuronal subset across all experimental conditions (43%, 9 out of 21 cells in home cage condition; 44%, 7 out of 16 cells in mice trained in VR with visual cues: 47%, 9 out of 19 cells in mice trained in VR without visual cues) (Figure 4B). These results reveal a modified axonal component in the AP waveform in fosGFP$^+$ cells which could result from a structural modification of the AIS. In order to test this hypothesis, we performed an immunofluorescent labelling for the scaffolding molecule ankyrin-G (AnkG) to quantify AIS length in fosGFP$^-$ and fosGFP$^+$ DCGs (Figure 5A). Experiments were performed *ex vivo* from mice maintained in home cage condition and from mice trained with or without visual cues (see above and Materials and Methods). The analysis was done in DGCs located in the outer part of the molecular layer of the DG (figure supplement 2B), since we showed that fosGFP$^+$ DGCs were preferentially distributed in this area across all experimental conditions (see above and Figure 2). We observed that fosGFP$^+$ DGCs displayed a similar shorter AIS length across all experimental conditions compared to fosGFP$^-$ DGCs (Figure 5C) (23 ± 0.67 µm in fosGFP$^-$ n = 47 vs 18.2 ± 0.6 µm in fosGFP$^+$ n = 47 in home cage condition, p<0.0001; 24.1 ± 0.63 µm in fosGFP$^-$ n = 57 vs 18.9 ± 0.62 µm in fosGFP$^+$ n = 57 in mice trained in VR with visual cues, p<0.0001; 23.1 ± 0.7 µm in fosGFP$^-$ n = 34 vs 18.5 ± 0.65 µm in fosGFP$^+$ n = 38 in mice trained in VR without visual cues, p<0.0001). This was due to a leftward shift of AIS length distribution towards smaller values (Figure 5B). Interestingly, the shorter AIS length is not associated with a significant relocation of AIS (Figure 5C).

Overall, our data reveal that a significant fraction of fosGFP$^+$ DGCs (when compared to fosGFP$^-$ DGCs) display a change in the dynamics of their AP waveform associated with a shorter AIS length, which is independent from the behavioural context of their activation.

Discussion

Our study performed *ex vivo* identifies subsets of mDGCs activated in different behavioural contexts (home cage condition and training with or without visual cues), using a fluorescent cellular tagging approach based on a transgenic mouse model in which the expression of EGFP is controlled by the promoter of the activity-dependent IEG *c-fos* (Barth et al., 2004). Our main finding is that activated mDGCs do not constitute a homogenous neuronal population in terms of intrinsic properties since they display different states of excitability depending on their context of activation. Remarkably, our data also reveal that activated mDGCs always exhibit lower excitability than the non-activated mDGCs across all experimental conditions. In keeping with this, our study shows that AIS length distribution is shifted towards lower values in activated mDGCs. This cellular mechanism could play a role in dampening their basal excitability as previously reported by *in vitro* experiments (Grubb and Burrone, 2010b).

It is well established that the expression of IEGs such as *c-fos* is selectively upregulated in subsets of neurons in specific brain regions associated with learning and memory formation (Minatohara et al., 2015). Notably, many studies have reported that, in these regions, neurons expressing an upregulation of *c-fos* encode and store informations required for memory recall (Minatohara et al., 2015; Tonegawa et al., 2015). Therefore, IEGs have been largely used to tag neurons involved in memory function and behavioural tasks. This enables targeting of sparse engram neurons (Tonegawa et al., 2015) to describe their functional features (Barth and Poulet, 2012). Using fosGFP mice, we identified *ex vivo* a sparse population of fosGFP$^+$ DGCs in the septal pole of the hippocampus activated in different behavioural contexts. Notably our findings revealed that training in VR with visual cues induces a significant increase in the number of fosGFP$^+$ DGCs compared with the home cage condition or training without visual cues. These data are in keeping with previous observations showing a sparse

recruitment of DGCs during a spatial behavioural experience (Chawla et al., 2005). Remarkably, we showed that, in all our experimental conditions, fosGFP$^+$ DGCs display features of mDGCs since (i) the examination of their radial distribution across the cell layer revealed a majority of fosGFP$^+$ cells located close to the molecular layer, and (ii) we did not observe cells that were co-labelled with EGFP and DCX antibodies. These observations reinforce the notion that mDGCs are not dormant cells (Alme et al., 2010) but comprise active neurons involved in specific tasks (Nakashiba et al., 2012; Vukovic et al., 2013).

We then questioned whether these subsets of mDGCs activated in the home cage condition or during training could have distinct electrophysiological properties. Indeed, there is a growing body of evidence showing that modulation of intrinsic excitability plays a central role in neuronal plasticity and learning processes (Barth, 2007; Daoudal and Debanne, 2003; Sehgal et al., 2013; Zhang and Linden, 2003). Most of the studies investigating a change in intrinsic excitability induced by learning have reported an increase in the firing rate (Daoudal and Debanne, 2003; Epsztein et al., 2011). Surprisingly, we observed an opposite scheme, as activated mDGCs display an overall lower intrinsic excitability than the non-activated cells. Besides this major observation, our findings reveal that activated DGCs do not constitute a homogenous population in terms of intrinsic properties since they exhibit different excitable states depending on the behavioural context of their activation. Indeed, we observed a significant higher excitability in activated DGCs from the mice trained with visual cues when compared to the cells from mice in home cage condition or trained without visual cues. Therefore, when comparing intrinsic properties of active neurons, our observations are in keeping with previous observations reporting an increase in excitability during training or learning processes (Daoudal and Debanne, 2003). We then observed that the difference in excitability is related to the value of input resistance. Indeed, in home cage condition activated mDGCs exhibit a much lower input resistance associated with a lower excitability

than the non-activated cells. Input resistance and excitability become significantly higher in activated mDGCs in trained mice but only when visual cues were available. Interestingly, in all experimental conditions this difference in input resistance is not associated with a significant change in RMP. Moreover, our data shows that glutamatergic and GABAergic ionotropic receptors are not involved in this phenomenon since we observe similar input resistances in activated DGCs in the absence or in the presence of AMPA and GABA-A receptor antagonists both in home cage and trained conditions. It is well established that input resistance is set by a variety of leak and voltage-dependent conductances and can be modulated by several intracellular signalling pathways (Lesage, 2003). Therefore, further experiments should be performed to elucidate the mechanisms involved in the setting of input resistance in mDGCs depending on their context of activation.

Another remarkable feature observed is the different dynamics of the phase plot of AP in activated DGCs compared to non-activated cells. Indeed, our data show that nearly all non-activated DGCs displayed a phase plot with two peaks accordingly to previous observations (Kress et al., 2008) across all experimental conditions. On the contrary, an important fraction (almost half) of activated DGCs display a phase plot where the first peak could not be detected by the analysis of the stationary inflection point (Kress et al., 2008). These data, that suggested a change in the axonal component of the AP waveform, could result from a structural modification of AIS. The AIS is a key element involved in the regulation of neuronal excitability since this cellular compartment is responsible for action potential initiation (Araki and Otani, 1955; Bean, 2007; Bender and Trussell, 2012; Coombs et al., 1957; Debanne et al., 2011; Grubb and Burrone, 2010a; Kole and Stuart, 2012; Petersen et al., 2016; Scott et al., 2014; Wefelmeyer et al., 2016). Moreover, it is now well accepted that AIS is not just a rigid structure but it continuously adapts to its surrounding environment. These changes occur on different time scales ranging from hours to days. AIS modifications can be

long-lasting, bidirectional, and are correlated with changes in intrinsic excitability (Evans et al., 2015; Grubb and Burrone, 2010b; Kuba et al., 2010; Wefelmeyer et al., 2016). A structural plasticity of AIS has been reported after several days in auditory nucleus neurons (Kuba et al., 2010). This plasticity, associated with alterations in excitability, contributes to long-term control of AP firing (Grubb and Burrone, 2010a; Kole and Stuart, 2012; Kuba et al., 2010; Wefelmeyer et al., 2015). The precise cellular mechanisms involved are not well understood but recent studies revealed that AIS plasticity depends on calcineurin signalling pathway (Evans et al., 2015). We now show that activated mDGCs display a shorter AIS length than the non-activated cells. As we observed similar reduced AIS length across all experimental conditions, we propose that this difference constitutes a common cellular signature of activated mDGCs independently of their context of activation, which could lead to an overall dampening of excitability via an homeostatic phenomenon (Wefelmeyer et al., 2016). Further experiments should be performed to clarify this point. We hypothesize that this prominent hypo-excitability could reinforce the sparse activity (Chawla et al., 2005; Diamantaki et al., 2016; Jung and McNaughton, 1993; Neunuebel and Knierim, 2012; Pilz et al., 2016; Skaggs et al., 1996; Stefanelli et al., 2016; Tonegawa et al., 2015) and the function of DGCs as coincidence detector (Schmidt-Hieber et al., 2007).

Taken together, our findings highlight a remarkable feature of activated mDGCs. We found that these neurons show different intrinsic properties depending on their behavioural contexts of activation, besides an overall dampening of excitability. We propose that these properties could constitute the neural signature of cell assemblies involved in specific contexts such as a familiar environment or spatial training.

Materials and methods

Mice

All experiments were approved by the National Institute of Health and Medical Research animal care and use agreement (D-13-055-19) and the European community council directive (2010/63/UE). Male adult (n = 91, 100 ± 3 days old, 25.7 ± 0.3 g) fosGFP heterozygous mice (B6.Cg-Tg (Fos/EGFP) 1-3Brth/J, Jackson Laboratory, Bar Harbor, ME; RRID = IMSR_JAX:014135) were used for experiments. These mice were generated by fusing the *c-fos* promoter and the *c-fos* coding region, including exons and introns, to the coding region for EGFP, creating a fosGFP C-terminus fusion protein (Barth et al., 2004). All mice were housed in standard conditions (12 hours light/dark cycles at 22 to 24°C, light off at 7:30 a.m., housed one per cage, and food ad libitum) and water restricted (see below). Mice were handled before recording sessions to limit stress and experiments were performed during the dark cycle.

Surgical procedures

After the mice being genotyped, a head-bar was implanted. For implantation fosGFP mice were anaesthetized with xylazine (13 mg/kg) / ketamine (66 mg/kg) in 0.9% saline and placed into a stereotactic frame. The skull was exposed and cleaned. Two screws were driven through small holes drilled in the bones and the head-bar was glued to the skull and fixed with bone cement (Heraeus Kulzer GmbH, Hanau, Germany). After 2-3 days of recovery animals were habituated to handling (1-2 days) and were water restricted (approximately 1 ml water/day). If mice weight dropped below 80% of pre-water restriction weight, they had access to food and water ad libitum and were discarded from the study.

Virtual reality set-up

Virtual reality (VR) offers unique advantages for studying whether visual cues are sufficient to drive learning of spatial navigation. Accordingly, in the present study we took advantage of VR to perform experiments in the presence or in the absence of visual cues. Mice were first habituated to be head-restrained on an air-flow-supported styrofoam ball and trained for 20-25 sessions (30 min per session, 2 sessions per day) (Phenosys GmbH; Berlin, Germany; Figure 1). Animals were running in a 150 cm-long linear track with visual cues on the side-walls (black dots, white dots, vertical green stripes and vertical black stripes) and distal visual cues on both sides provided through six TFT monitors surrounding the animal (JetBall-TFT, Phenosys GmbH), allowing them to identify their position throughout the linear track. Although mice were allowed to move the JetBall in all directions, only the movements along the long axis of the maze were recorded by the system. Upon arrival to the end of the maze, the ball was immobilized by brakes and mice received a small (approx. 4 µl) water drop through a delivery tube; consecutive rewards at the same end were not available. After having obtained the reward, mice were then able to go back by turning the jet-ball to reach the next reward. When the animals performed sufficient number of session (20-25), they were anaesthetised with xylazine (13 mg/kg) / ketamine (66 mg/kg) and sacrificed. Analyses of the speed of the mice along the linear track and quantification of the number of rewards were performed *a posteriori* using custom-developed softwares written in MATLAB (MathWorks, Natick, MA).

Quantification of fosGFP^{+} cells

After completion of behaviour, mice were deeply anesthetized with xylazine (13 mg/kg) / ketamine (66 mg/kg) prior to decapitation. The brain was then rapidly removed and hippocampi were dissected and fixed overnight (home cage: n = 6 mice, trained in VR with

cues: n = 5 mice, trained in VR without cues: n = 4 mice). Transverse 80 µm thick slices were cut using a Leica VT1000S vibratome (Leica Microsystems, Wetzlar, Germany). Slices were then permeabilized in blocking solution containing 5% normal goat serum (NGS, Sigma-Aldrich, Merck KGaA, Darmstadt, Germany) in 0.5% Triton for 1 hour at room temperature. Slices were then incubated in the polyclonal rabbit anti-EGFP antibody (Fisher Scientific, Hampton, NH) at 1:1000 in 5% NGS in 0.5% Triton overnight at 4°C. Slices were then incubated for 2 hours in secondary antibody Alexa488 (Invitrogen, Carlsbad, CA, 1:500) and counterstained with Neurotracer fluorescent Nissl (Invitrogen; RRID:AB_2620170) at 1:250 then coverslipped in fluoro-gel (Electron Microscopy Sciences, Hatfield, PA). Immunofluorescence was visualized using a confocal microscope (TCS SP5 X, Leica Microsystems) and analysis of traced DG area was assessed by using ImageJ (NIH). We confirmed that expression of the fosGFP transgene correlated with the expression of the endogenous c-fos protein using a c-fos specific antibody (Synaptic Systems GmbH, Göttingen, Germany; RRID: AB_2106755, see below); we found that almost all fosEGFP$^+$ neurons were co-labelled with EGFP and c-fos antibodies (100 %, n = 18 cells, n = 2 mice in home cage condition; 89.7 %, n = 146 cells, n = 3 mice trained with visual cues; 100 %, n = 61 cells, n = 2 mice trained without visual cues) (figure supplement 1A). The percentage of fosGFP$^+$ cells was calculated by using the total number of granule cells in the DG (Buckmaster and Wen, 2011) and the volume of the DG (van Praag et al., 1999). Then, the percentage was measured by calculating the number of fosGFP$^+$ cells/mm^3 reported to the total number of granule cells/mm^3 (967 442 cells/mm^3). The spatial distribution of fosGFP$^+$ cells was measured manually. We defined the tip of DG lower blade as 0 and that of DG upper blade as 1 in the lateral direction and the border between granule cell layer and the hilus as 0 and that between granule cell layer and molecular layer as 1 in the radial direction and then plotted the count and distribution of fosGFP$^+$ cells.

Immunohistochemistry

Slices were fixed then permeabilized in blocking solution containing 5% normal goat serum (NGS) (Sigma-Aldrich) and 0.5% Triton for 1 hour at room temperature. The slices were incubated with polyclonal chicken anti-EGFP (Abcam, Cambridge, UK; RRID:AB_300798) at 1:1000 and either with polyclonal Guinea pig anti-c-fos antibody (Synaptic Systems; RRID: AB_2106755) at 1:500 or polyclonal rabbit anti-Prox1 antibody (Millipore; Merck KGaA, Darmstadt, Germany, RRID:AB_177485) at 1:2000 or polyclonal rabbit anti-DCX antibody (Abcam; RRID:AB_2088478) at 1:1000 in 5% NGS in 0.5% Triton overnight at 4°C. Slices were then incubated for 2 hours in secondary antibody Alexa488 or Alexa555 (Invitrogen 1:500) and then coverslipped in fluoro-gel. Specific protocol has been used for Ankyrin G immunostaining (NeuroMab; UC Davis/NIH NeuroMab Facility, Davis, CA; RRID: AB_10673030). Trained mice were first deeply anesthetized with an i.p. injection of xylazine (13 mg/kg) / ketamine (66 mg/kg), then briefly intracardiacally perfused (flowrate: 8–10 ml/min for 2–5 min) with cold 1X phosphate buffer (PBS, pH 7.4), followed by 10 min of cold 1% antigenfix (Diapath, Martinengo, Italy). Brains were removed carefully and post-fixed in antigenfix for 24 h at 4°C and then cryopreserved in 20–30% sucrose / PBS at 4°C. Brains were allowed to completely sink to the bottom of the container before sectioning. Then, they were embedded in OCT compound (Tissue-Tek R, TedPella Inc., Redding, CA) and placed at -80°C. Frozen brains were sectioned transversally into 30 μm thick slices at −20°C to −25°C using a Leica CM 3050S cryostat (Leica Microsystems). Floating brain sections were washed with 1X PBS, and then pre-incubated with permeabilizing agent containing 0.5% Triton, 0.2% Tween-20 and 3% BSA. Then slices were washed with 0.2% Tween-20 and incubated with a blocking buffer consisting of 5% NGS (Sigma-Aldrich) and monoclonal mouse anti-ankyrinG antibody (1:500) (NeuroMab) overnight at 4°C. Slices were washed and incubated with biotin-conjugated secondary antibody (1:500) (Invitrogen)

followed by incubation with Cy3-conjugated streptavidin (1:500) (Sigma Aldrich), then coverslipped with mounting medium containing DAPI (Vector laboratories, Burlingame, CA). Image acquisition with a Leica confocal microscope was performed to associate each AIS labelled with anti-ankyrinG antibody with the corresponding fosGFP$^+$ cell via EGFP staining and fosGFP$^-$ cell via DAPI staining. These images were also used for the reconstruction of the soma and the AIS with Neurolucida software. Image acquisition with a Leica confocal microscope (40 X oil immersion objective; using a laser scanning with appropriate excitation and emission filters) was performed to associate each AIS labelled with anti-ankyrinG antibody with the corresponding fosGFP$^+$ cell via EGFP staining and fosGFP$^-$ cell via DAPI staining. These images were also used for a 3D-reconstruction of the soma and the AIS with Neurolucida software. The 'start' and 'end' positions of AIS were the proximal and distal axonal points, respectively, at which the fluorescence profile dipped to 33% of its maximum peak (figure supplement 2A) (Grubb and Burrone, 2010a).

Acute slice preparation

Hippocampal slices were prepared from heterozygous fosGFP mice. The slices were cut 45 min after the last training session in VR (20-25 sessions). Animals were deeply anesthetized with xylazine (13 mg/kg) / ketamine (66 mg/kg) prior to decapitation. The brain was then rapidly removed, and transverse 350 µm thick slices were cut using a Leica VT1200S vibratome in ice-cold oxygenated (95% O_2 and 5% CO_2) modified artificial cerebrospinal fluid (ACSF) containing the following (in mM): 132 choline, 2.5 KCl, 1.25 NaH_2PO_4, 25 $NaHCO_3$, 7 $MgCl_2$, 0.5 $CaCl_2$, and 8 D-glucose. Slices were transferred to rest at room temperature in oxygenated (95% O_2 and 5% CO_2) solution of ACSF containing the following (in mM): 126 NaCl, 3.5 KCl, 1.2 NaH_2PO_4, 26 $NaHCO_3$, 1.3 $MgCl_2$, 2.0 $CaCl_2$, and 10 D-glucose, pH 7.4.

Electrophysiological recordings

Individual slices were transferred to an upright microscope and neurons were visualized with infrared differential interference contrast microscopy (SliceScope Pro 3000M, Scientifica, Uckfield, UK). Slices were placed in a submerged chamber and perfused with oxygenated ASCF (30-32°C) at a flow rate of 2 to 3 ml/min. Whole cell recordings of DGCs were obtained using patch clamp technique. Glass electrodes (resistance 6-8 MΩ) were filled with an internal solution containing the following (in mM): 130 $KMeSO_4$, 5 KCl, 10 4-(2-hydroxyethyl)-1-piperazi-methanesulfonic acid, 2.5 MgATP, 0.3 NaGTP, 0.2 ethyleneglycoltetraacetic acid, 10 phosphocreatine, and 0.3 to 0.5% biocytin, pH 7.25. Access resistance ranged between 15 and 30 MΩ, and the results were discarded if the access resistance changed by >20%. Whole cell recordings were performed in current-clamp mode using a Multiclamp 700B amplifier (Molecular Devices, Sunnyvale, CA). Data were filtered at 2 kHz, digitized (20 kHz) with a Digidata 1440A (Molecular Devices) to a personal computer, and acquired using Clampex 10.1 software (PClamp, Molecular Devices). The recordings alternated between targeting $fosGFP^-$ and $fosGFP^+$ neurons during the course of an experiment. To avoid EGFP bleaching, the tissue was illuminated for a short period of time, typically around 5-10 s, to focus and record the image of targeted neuron.

Electrophysiological parameters were tested at least 5 min after whole-cell was established and resting membrane potential (RMP) was stable for at least 5 min. Electrophysiological parameters were measured from responses to step current injections (500 ms duration) increasing from negative to positive values, and applied from a fixed membrane potential of -60 mV. Input resistance (Rin) was determined by plotting the membrane potential variations induced by hyperpolarising 500 ms steps of current (from -60 pA to 0 pA) and measuring the slope of the fitted linear regression curve. Firing frequency was studied by injecting 500 ms pulses of depolarizing current (I: from 20 pA up to 120 pA) into the cell and plotting the spike

frequency (f) as a function of the current intensity (f/I plot). The AP waveform was analysed on the first AP elicited at suprathreshold potential (Mini Analysis Program, Synaptosoft, Decatur, GA). AP threshold was defined as the membrane potential when dV/dt > 10 mV/ms (Kress et al., 2008; Naundorf et al., 2006). AP amplitude was the difference between the AP threshold and the AP peak. AP width was measured from the half-height of the AP amplitude. Second-derivative (denoted d^2V/dt^2) of the somatic membrane potential was calculated using Clampfit analysis tools. Phase plots were constructed by plotting d^2V/dt^2 as a function of somatic membrane potential. Stationary inflection point refers to the point where the second derivative displays a slope of zero (Kress et al., 2008). Gabazine (SR-95531) and NBQX were purchased from Tocris Bioscience (Bristol, UK).

Statistical analysis

All values are given as means ± SEM. Statistical analyses were performed using Graphpad Prism 7 (GraphPad Software, La Jolla, CA). For comparison between groups with normal distribution, the two-sample unpaired Student's t test was used for two groups. When data were not normally distributed, the unpaired Mann–Whitney rank-sum test was used. The χ^2 or the Fisher's exact tests were used to compare proportions. For comparison of groups with dependent variables, ANOVA was used. Statistics are shown in the text and the supplementary table.

Acknowledgments

We thank B. Poucet, D. Robbe, A. Malvache, J. Epsztein, J. Koenig, I. Bureau, R. Cossart, A. Represa, R. Khazipov, S. X. Ho, and T. Marissal for helpful comments on this manuscript; and S. Varpula, S. Moussa, T. Tressard, and L. Petit for technical assistances. S. Corby-Pellegrino for heading the animal house facility. This work was supported by the Institut

National de la Santé et de la Recherche Médicale (INSERM), Aix-Marseille Université (AMU), the Agence Nationale de la Recherche (ANR) (ANR 13-BSV4-0012-02 to V.C.), and the french Ministère de l'Enseignement Supérieur et de la Recherche (MESR to C.P.).

Competing interests

No competing interests

References

Aimone, J.B., Deng, W., and Gage, F.H. (2011). Resolving new memories: a critical look at the dentate gyrus, adult neurogenesis, and pattern separation. Neuron *70*, 589–596.

Alme, C.B., Buzzetti, R. A., Marrone, D.F., Leutgeb, J.K., Chawla, M.K., Schaner, M.J., Bohanick, J.D., Khoboko, T., Leutgeb, S., Moser, E.I., et al. (2010). Hippocampal granule cells opt for early retirement. Hippocampus *20*, 1109–1123.

Altman, J., and Bayer, S.A. (1990). Migration and distribution of two populations of hippocampal granule cell precursors during the perinatal and postnatal periods. J. Comp. Neurol. *301*, 365–381.

Araki, T., and Otani, T. (1955). Response of single motoneurons to direct stimulation in toad's spinal cord. J. Neurophysiol. *18*, 472–485.

Barth, A.L. (2007). Visualizing circuits and systems using transgenic reporters of neural activity. Curr. Opin. Neurobiol. *17*, 567–571.

Barth, A.L., and Poulet, J.F.A. (2012). Experimental evidence for sparse firing in the neocortex. Trends Neurosci. *35*, 345–355.

Barth, A.L., Gerkin, R.C., and Dean, K.L. (2004). Alteration of neuronal firing properties after in vivo experience in a FosGFP transgenic mouse. J. Neurosci. *24*, 6466–6475.

Bean, B.P. (2007). The action potential in mammalian central neurons. Nat. Rev. Neurosci. *8*,

451–465.

Bender, K.J., and Trussell, L.O. (2012). The physiology of the axon initial segment. Annu. Rev. Neurosci. *35*, 249–265.

Buckmaster, P.S., and Wen, X. (2011). Rapamycin suppresses axon sprouting by somatostatin interneurons in a mouse model of temporal lobe epilepsy. Epilepsia *52*, 2057–2064.

Cameron, H.A., and Mckay, R.D.G. (2001). Adult neurogenesis produces a large pool of new granule cells in the dentate gyrus. J. Comp. Neurol. *435*, 406–417.

Chawla, M.K., Guzowski, J.F., Ramirez-Amaya, V., Lipa, P., Hoffman, K.L., Marriott, L.K., Worley, P.F., McNaughton, B.L., and Barnes, C. A. (2005). Sparse, environmentally selective expression of Arc RNA in the upper blade of the rodent fascia dentata by brief spatial experience. Hippocampus *15*, 579–586.

Clelland, C.D., Choi, M., Romberg, C., Clemenson, G.D., Fragniere, A., Tyers, P., Jessberger, S., Saksida, L.M., Barker, R.A., Gage, F.H., et al. (2009). A functional role for adult hippocampal neurogenesis in spatial pattern separation. Science *325*, 210–213.

Colbert, C.M., and Johnston, D. (1996). Axonal action-potential initiation and Na+ channel densities in the soma and axon initial segment of subicular pyramidal neurons. J. Neurosci. *16*, 6676–6686.

Coombs, J.S., Curtis, D.R., and Eccles, J.C. (1957). The generation of impulses in motoneurones. J. Physiol. *139*, 232–249.

Czajkowski, R., Jayaprakash, B., Wiltgen, B., Rogerson, T., Guzman-Karlsson, M.C., Barth, A.L., Trachtenberg, J.T., and Silva, A.J. (2014). Encoding and storage of spatial information in the retrosplenial cortex. Proc. Natl. Acad. Sci. *111*, 8661–8666.

Daoudal, G., and Debanne, D. (2003). Long-term plasticity of intrinsic excitability: learning rules and mechanisms. Learn. Mem. *10*, 456–465.

Debanne, D., Campanac, E., Bialowas, A., Carlier, E., and Alcaraz, G. (2011). Axon

physiology. Physiol. Rev. *91*, 555–602.

Diamantaki, M., Frey, M., Berens, P., Preston-Ferrer, P., and Burgalossi, A. (2016). Sparse activity of identified dentate granule cells during spatial exploration. Elife *5*, 1–17.

Dombeck, D. A, Harvey, C.D., Tian, L., Looger, L.L., and Tank, D.W. (2010). Functional imaging of hippocampal place cells at cellular resolution during virtual navigation. Nat. Neurosci. *13*, 1433–1440.

Epsztein, J., Brecht, M., and Lee, A.K. (2011). Intracellular Determinants of Hippocampal CA1 Place and Silent Cell Activity in a Novel Environment. Neuron *70*, 109–120.

Evans, M.D., Dumitrescu, A.S., Kruijssen, D.L.H., Taylor, S.E., Grubb (2015). Rapid Modulation of Axon Initial Segment Length Influences Repetitive Spike Firing. CellReports *13*, 1–13.

Fuortes, M.G., Frank, K., and Becker, M.C. (1957). Steps in the production of motoneuron spikes. J. Gen. Physiol. *40*, 735–752.

Grace, A.A., and Bunney, B.S. (1983). Intracellular and extracellular electrophysiology of nigral dopaminergic neurons--1. Identification and characterization. Neuroscience *10*, 301–315.

Grubb, M.S., and Burrone, J. (2010a). Activity-dependent relocation of the axon initial segment fine-tunes neuronal excitability. Nature *465*, 1070–1074.

Grubb, M.S., and Burrone, J. (2010b). Building and maintaining the axon initial segment. Curr. Opin. Neurobiol. *20*, 481–488.

Harvey, C.D., Collman, F., Dombeck, D. A, and Tank, D.W. (2009). Intracellular dynamics of hippocampal place cells during virtual navigation. Nature *461*, 941–946.

Häusser, M., Stuart, G., Racca, C., and Sakmann, B. (1995). Axonal initiation and active dendritic propagation of action potentials in substantia nigra neurons. Neuron *15*, 637–647.

Hölscher, C., Schnee, A., Dahmen, H., Setia, L., and Mallot, H.A. (2005). Rats are able to

navigate in virtual environments. J. Exp. Biol. *208*, 561–569.

Jung, M.W., and McNaughton, B.L. (1993). Spatial selectivity of unit activity in the hippocampal granular layer. Hippocampus *3*, 165–182.

Kempermann, G., Kuhn, H.G., and Gage, F.H. (1997). Genetic influence on neurogenesis in the dentate gyrus of adult mice. Proc. Natl. Acad. Sci. U. S. A. *94*, 10409–10414.

Kole, M.H.P., and Stuart, G.J. (2012). Signal Processing in the Axon Initial Segment. Neuron *73*, 235–247.

Kress, G.J., Dowling, M.J., Meeks, J.P., and Mennerick, S. (2008). High threshold, proximal initiation, and slow conduction velocity of action potentials in dentate granule neuron mossy fibers. J. Neurophysiol. *100*, 281–291.

Kropff, E., Yang, S.M., and Schinder, A.F. (2015). Dynamic role of adult-born dentate granule cells in memory processing. Curr. Opin. Neurobiol. *35*, 21–26.

Kuba, H., Oichi, Y., and Ohmori, H. (2010). Presynaptic activity regulates Na(+) channel distribution at the axon initial segment. Nature *465*, 1075–1078.

Lesage, F. (2003). Pharmacology of neuronal background potassium channels. Neuropharmacology *44*, 1–7.

Leutgeb, J.K., Leutgeb, S., Moser, M.-B., and Moser, E.I. (2007). Pattern separation in the dentate gyrus and CA3 of the hippocampus. Science *315*, 961–966.

Lopez-Rojas, J., and Kreutz, M.R. (2016). Mature granule cells of the dentate gyrus—Passive bystanders or principal performers in hippocampal function? Neurosci. Biobehav. Rev. *64*, 167–174.

McNaughton, B.L., and Morris, R.G.M. (1987). Hippocampal synaptic enhancement and information storage within a distributed memory system. Trends Neurosci. *10*, 408–415.

Meeks, J.P., and Mennerick, S. (2007). Action potential initiation and propagation in CA3 pyramidal axons. J. Neurophysiol. *97*, 3460–3472.

Minatohara, K., Akiyoshi, M., and Okuno, H. (2015). Role of Immediate-Early Genes in Synaptic Plasticity and Neuronal Ensembles Underlying the Memory Trace. Front. Mol. Neurosci. *8*, 78.

Moser, E., Moser, M.B., and Andersen, P. (1993). Spatial learning impairment parallels the magnitude of dorsal hippocampal lesions, but is hardly present following ventral lesions. J. Neurosci. *13*, 3916–3925.

Nakashiba, T., Cushman, J.D., Pelkey, K. A., Renaudineau, S., Buhl, D.L., McHugh, T.J., Barrera, V.R., Chittajallu, R., Iwamoto, K.S., McBain, C.J., et al. (2012). Young dentate granule cells mediate pattern separation, whereas old granule cells facilitate pattern completion. Cell *149*, 188–201.

Naundorf, B., Wolf, F., and Volgushev, M. (2006). Unique features of action potential initiation in cortical neurons. Nature *440*, 1060–1063.

Neunuebel, J.P., and Knierim, J.J. (2012). Spatial Firing Correlates of Physiologically Distinct Cell Types of the Rat Dentate Gyrus. J. Neurosci. *32*, 3848–3858.

Neunuebel, J.P., and Knierim, J.J. (2014). CA3 retrieves coherent representations from degraded input: Direct evidence for CA3 pattern completion and dentate gyrus pattern separation. Neuron *81*, 416–427.

Ninkovic, J., Mori, T., and Gotz, M. (2007). Distinct modes of neuron addition in adult mouse neurogenesis. J. Neurosci. *27*, 10906–10911.

Petersen, A.V., Cotel, F., and Perrier, J.-F. (2016). Plasticity of the Axon Initial Segment: Fast and Slow Processes with Multiple Functional Roles. The Neuroscientist *23*, 364-373

Pilz, G.-A., Carta, S., Stäuble, A., Ayaz, A., Jessberger, S., and Helmchen, F. (2016). Functional Imaging of Dentate Granule Cells in the Adult Mouse Hippocampus. J. Neurosci. *36*, 7407–7414.

Praag, H A., Kempermann, G., and Gage, F.H. (1999). Running increases cell proliferation

and neurogenesis in the adult mouse dentate gyrus. Nat. Neurosci. *2*, 266–270.

Ravassard, P., Kees, A., Willers, B., Ho, D., Aharoni, D., Cushman, J., Aghajan, Z.M., and Mehta, M.R. (2013). Multisensory Control of Hippocampal Spatiotemporal Selectivity. Science (80-.). *340*, 1342–1346.

Sahay, A., Scobie, K.N., Hill, A.S., O'Carroll, C.M., Kheirbek, M. A, Burghardt, N.S., Fenton, A. A, Dranovsky, A., and Hen, R. (2011). Increasing adult hippocampal neurogenesis is sufficient to improve pattern separation. Nature *472*, 466–470.

Schmidt-Hieber, C., Jonas, P., and Bischofberger, J. (2007). Subthreshold dendritic signal processing and coincidence detection in dentate gyrus granule cells. J. Neurosci. *27*, 8430–8441.

Scott, R.S., Henneberger, C., Padmashri, R., Anders, S., Jensen, T.P., and Rusakov, D.A. (2014). Neuronal adaptation involves rapid expansion of the action potential initiation site. Nat. Commun. *5*, 3817.

Sehgal, M., Song, C., Ehlers, V.L., and Moyer, J.R. (2013). Learning to learn - intrinsic plasticity as a metaplasticity mechanism for memory formation. Neurobiol. Learn. Mem. *105*, 186–199.

Skaggs, W.E., McNaughton, B.L., Wilson, M. A., and Barnes, C. A. (1996). Theta phase precession in hippocampal neuronal populations and the compression of temporal sequences. Hippocampus *6*, 149–172.

Stefanelli, T., Bertollini, C., Lüscher, C., Muller, D., and Mendez, P. (2016). Hippocampal Somatostatin Interneurons Control the Size of Neuronal Memory Ensembles. Neuron *89*, 1074–1085.

Tonegawa, S., Liu, X., Ramirez, S., and Redondo, R. (2015). Memory Engram Cells Have Come of Age. Neuron *87*, 918–931.

Vukovic, J., Borlikova, G.G., Ruitenberg, M.J., Robinson, G.J., Sullivan, R.K.P., Walker,

T.L., and Bartlett, P.F. (2013). Immature doublecortin-positive hippocampal neurons are important for learning but not for remembering. J. Neurosci. *33*, 6603–6613.

Wefelmeyer, W., Cattaert, D., and Burrone, J. (2015). Activity-dependent mismatch between axo-axonic synapses and the axon initial segment controls neuronal output. Proc. Natl. Acad. Sci. U. S. A. *112*, 9757–9762.

Wefelmeyer, W., Puhl, C.J., and Burrone, J. (2016). Homeostatic Plasticity of Subcellular Neuronal Structures: From Inputs to Outputs. Trends Neurosci. *39*, 656–667.

Youngstrom, I. A., and Strowbridge, B.W. (2012). Visual landmarks facilitate rodent spatial navigation in virtual reality environments. Learn. Mem. *19*, 84–90.

Zhang, W., and Linden, D.J. (2003). The other side of the engram: experience-driven changes in neuronal intrinsic excitability. Nat. Rev. Neurosci. *4*, 885–900.

Zhao, C., Deng, W., and Gage, F.H. (2008). Mechanisms and functional implications of adult neurogenesis. Cell *132*, 645–660.

Figure legends

Figure 1. Increased number in fosGFP$^+$ neurons in mice trained with visual cues

(A) Schematic representation of the experimental set-up. Mice were fixed to an arm with a screw through a chronically implanted head-bar. By moving an air-flow-supported styrofoam JetBall, mice were navigating in a virtual environment provided through six TFT monitors surrounding the JetBall (270°). Reward was delivered to the animal through a plastic tube.

(B) Screenshots from the middle to the right and left ends of the track. The track (150 cm) was divided into four regions with different textures (black dots, white dots, vertical green stripes and vertical black stripes). Water rewards were given at the ends of the track, with available rewards alternating between reward sites.

(C) Sample trajectories for an individual mouse on training sessions 2 and 20; position is the animal's location along the 150 cm-long linear track axis and blue dots indicate rewards (left panel). Rate of rewards vs. session numbers for mice trained with (green) or without (red) visual cues (middle panel). Running speed of mice as a function of the position on the linear track for mice trained with (green) or without (red) visual cues (right panel). Grey box represent the deceleration zone (from 120 to 150 cm).

(D) On the top, schematic of the three different experimental conditions: home cage, training in VR with or without visual cues. On the bottom: Nissl staining (red) of septal DG with an immunostaining using anti-EGFP antibody (green); scale bar 100 µm. Insets show parts of septal DG at higher magnification; scale bar 50 µm.

(E) Bar graphs displaying the percentage of fosGFP$^+$ cells activated in septal DG in mice in home cage (H.C.), mice trained with (T.w/.C.) or without (T.w/o.C.) visual cues.

Data are shown as mean ± SEM. *$p<0.05$, ***$p<0.0001$, ns, $p>0.05$. In this and following figures the statistics are shown in the supplementary table.

Figure 2. fosGFP$^+$ cells display characteristics of mature DGCs

(A) Top: Schematic illustration of DG from confocal image of Figure 1D with fosGFP$^+$ cells represented as solid circles. Bottom: Plot diagram representing lateral and radial distributions of fosGFP$^+$ from septal DG in mice in home cage (HC, triangles), trained with (T.w/.C., circles) or without (T.w/o.C., diamonds) visual cues. The tip of lower blade of granule cell layer is defined as 0 and that of upper blade as 1 in the lateral direction. The border between granule cell layer and the hilus is defined as 0 (int. for internal) and that between granule cell layer and molecular layer (ml) as 1 (ext. for external) in the radial direction. The histograms above and on the right of the square diagram indicate the number of fosGFP$^+$ cells in the lateral and radial direction, respectively.

(B) Bar graph of the percentage of localization of fosGFP$^+$ cells for radial (int. vs ext.) and lateral (lower vs upper) distributions in H.C., T.w/.C and T.w/o.C. conditions. Data are shown as mean ± SEM. ***p<0.0001.

(C) Top: Representative double immunostaining using anti-EGFP antibody associated with anti-Prox1. Bottom: Representative double immunostaining using anti-EGFP antibody associated with anti-DCX; scale bar 10 µm.

Figure 3. fosGFP$^+$ DGCs display different intrinsic properties

(A) Representative membrane potential variation and action potential discharges evoked in fosGFP$^-$ or fosGFP$^+$ DGCs in mice in home cage (H.C.) (top), trained with (T. w/.C.) (middle) or without (bottom) visual cues (T.w/o.C.) evoked by 500 ms current steps varying from -60 pA to +120 pA by 20 pA step increments, at a holding potential of -60 mV.

(B) Linear regression curves (solid lines, dashed lines are for error interval) fitted for the mean discharge frequency/injected current relationship (symbols) of fosGFP$^-$ and fosGFP$^+$ DGCs in H.C. (triangle), T.w/.C. (square) and T.w/o.C. (diamond) conditions.

(C) Bar graphs displaying the firing gain, (D) the input resistance, and (E) rheobase of fosGFP$^-$ and fosGFP$^+$ DGCs in each condition. Note that the f/I plots, the gain, the input resistance, and the rheobase are significantly different when comparing fosGFP$^-$ with fosGFP$^+$ DGCs, and when comparing fosGFP$^+$ DGCs in H.C. with fosGFP$^+$ DGCs in T.w/.C. conditions. Data are shown as mean ± SEM. *p<0.05, **p<0.01, ***p<0.0001, ns, p>0.05.

Figure 4. fosGFP$^+$ DGCs display a modified AP waveform

(A) Representative superimposed phase plots of the 2nd derivative of the somatic membrane potential (d^2V/dt^2) vs. membrane potential (Vm) of action potentials recorded in fosGFP$^-$ and fosGFP$^+$ DGCs in mice in home cage (H.C.), trained with (T.w/.C.) or without (T.w/o.C.)

visual cues; threshold has been taken as reference. Top: phase plots of action potential with two peaks (the first one reflecting the spike initiation in AIS and the second one the somato-dendritic spike). Bottom: phase plots of action potential showing only one peak, the somato-dendritic component.

(B) Pie charts of distribution of phase plots with 1 (plain area) or 2 (striped area) peaks in fosGFP$^-$ and fosGFP$^+$ DGCs in each condition. Note that about 90% of fosGFP$^-$ DGCs display two peaks, whereas about 50% of fosGFP$^+$ DGCs display only one peak.

Figure 5. fosGFP$^+$ DGCs display a shorter AIS length

(A) Projection of confocal images of fosGFP$^-$ (left) and fosGFP$^+$ (right) DGCs showing immunostaining using anti-EGFP, anti-Ankyrin-G antibodies and DAPI and their Neurolucida reconstructions in mice in home cage (H.C., top), trained with (T.w/.C., middle) or without (T.w/o.C., bottom) visual cues ; scale bar, 5 µm.

(B) AIS length distribution of fosGFP$^-$ (left) or fosGFP$^+$ (right) DGCs in H.C. (top), T.w/.C. (middle) and T.w/o.C. (bottom) conditions; m indicates the value of the median of the Gaussian fit. Note the shift of AIS length distribution towards smaller values when comparing fosGFP$^+$ to fosGFP$^-$ cells.

(C) Bar graphs displaying the AIS length (left) and the distance from the soma (right) of fosGFP$^-$ and fosGFP$^+$ DGCs in H.C., T.w/.C. and T.w/o.C. conditions. Note that the length of AIS is significantly shorter in fosGFP$^+$ DGCs. Data are shown as mean ± SEM. ***$p<0.0001$, ns, $p>0.05$.

Table

Intrinsic electrophysiological properties of fosGFP$^-$ and fosGFP$^+$ DGCs in all conditions.

H.C.								
		Gain (AP frq/pA)	**R input (MΩ)**	**Rheobase (pA)**	RMP (mV)	AP amp (mV)	Threshold (mV)	AP (HW)
fosGFP$^-$	Mean	**0.37**	**343.1**	**35.2**	-77.4	75.98	-42.5	1.2
	sem	**0.04**	**21.91**	**2.36**	1.01	2.24	1.31	0.04
	n	**29**	**29**	**29**	22	29	29	29
fosGFP$^+$	Mean	**0.12**	**191.0**	**82.9**	-74.4	69.8	-38.7	1.3
	sem	**0.02**	**11.96**	**9.79**	1.13	2.93	1.71	0.07
	n	**18**	**21**	**21**	17	21	21	21
	p	**<0.0001 Mann-Whitney**	**<0.0001 Mann-Whitney**	**<0.0001 Mann-Whitney**	0.0523 Unpaired t test	0.0958 Unpaired t test	0.0703 Mann-Whitney	0.3684 Mann-Whitney
T.w/.C.								
		Gain (AP frq/pA)	**R input (MΩ)**	**Rheobase (pA)**	RMP (mV)	AP amp (mV)	Threshold (mV)	AP (HW)
fosGFP$^-$	Mean	**0.37**	**340.47**	**30.77**	-78.95	77.06	-41.28	1.19
	SEM	**0.03**	**12.16**	**2.28**	1.26	1.73	0.88	0.03
	n	**26**	**26**	**26**	25	26	26	26
fosGFP$^+$	Mean	**0.21**	**254.06**	**43.75**	-77.86	70.75	-39.47	1.22
	sem	**0.03**	**22.96**	**4.17**	1.57	2.83	1.69	0.08
	n	**16**	**16**	**16**	14	16	16	16
	p	**0.002 Unpaired t test**	**<0.0001 Mann-Whitney**	**0.0096 Mann-Whitney**	0.8002 Mann-Whitney	0.0504 Unpaired t test	0.2984 Unpaired t test	0.6485 Unpaired t test
T.w/o.C.								
		Gain (AP frq/pA)	**R input (MΩ)**	**Rheobase (pA)**	RMP (mV)	AP amp (mV)	Threshold (mV)	AP (HW)
fosGFP$^-$	Mean	**0.34**	**356.4**	**27.5**	-75.0	79.1	-43.8	1.3
	sem	**0.04**	**26.47**	**3.66**	2.48	6.50	3.14	0.06
	n	**8**	**8**	**8**	7	8	8	8
fosGFP$^+$	Mean	**0.13**	**194.5**	**72.0**	-72.9	73.1	-41.7	1.4
	sem	**0.02**	**12.36**	**8.99**	1.52	2.59	1.68	0.07
	n	**17**	**20**	**20**	19	20	20	20
	p	**<0.0001 Unpaired t test**	**<0.0001 Unpaired t test**	**0.0003 Mann-Whitney**	0.4651 Unpaired t test	0.3117 Unpaired t test	0.6637 Mann-Whitney	0.1121 Mann-Whitney

Supplementary figure 1

(A) Representative double immunostaining using anti-EGFP antibody associated with anti-c-fos in mice in home cage (H.C), trained with (T.w/.C.) or without (T.w/o.C.) visual cues; scale bar 10 µm.

(B) Representative double immunostaining using anti-EGFP antibody associated with anti-Prox1 in each condition; scale bar 10 µm.

(C) Representative double immunostaining using anti-EGFP antibody associated with anti-DCX in each condition; scale bar 10 µm.

Supplementary figure 2

(A) Top, projection of a confocal image showing immunostaining using anti-Ankyrin-G antibodies and DAPI and the superimposed Neurolucida reconstructions of the soma (dotted line) and axon initial segment (solid line); scale bar, 5 µm. Bottom, fluorescence intensity along the axon initial segment.

(B) Bar graphs displaying the normalized radial position of fosGFP^{-} and fosGFP^{+} cells used to analyse AIS length and AIS location from the soma in mice in home cage (H.C.), trained with (T.w/.C.) or without (T.w/o.C.) visual cues. Data are shown as mean ± SEM. ns, $p>0.05$.

Supplementary table

Figure	Panel	Variables	Test	n	p
Fig1	C	# Reward/min T. w/. C. vs T. w/o. C.	Two-way ANOVA	9 mice T. w/. C., 8 mice T. w/o. C.	0.2297
Fig1	C	Speed (cm/s) from 0 to 120 cm T. w/. C. vs T. w/o. C.	Two-way ANOVA	8 mice T. w/. C., 8 mice T. w/o. C.	0.9414
Fig1	C	Speed (cm/s) in the deceleration zone (from 120 to 150 cm) T. w/. C. vs T. w/o. C.	Two-way ANOVA	8 mice T. w/. C., 8 mice T. w/o. C.	0.0387
Fig1	E	% cell fosGFP$^+$ H.C. vs T. w/. C	Unpaired t test	6 mice H.C., 25 slices H.C., 5 mice T. w/. C., 19 slices T. w/. C.,	< 0.0001
Fig1	E	% cell fosGFP$^+$ T. w/. C. vs T. w/o. C.	Unpaired t test	5 mice T. w/. C., 19 slices T. w/. C., 4 mice T. w/o. C., 13 slices T. w/o. C.	0.0002
Fig1	E	% cell fosGFP$^+$ H.C. vs T. w/o. C.	Unpaired t test	6 mice H.C., 25 slices H.C., 4 mice T. w/o. C., 13 slices T. w/o. C.	0.4081
Fig2	B	Internal vs External H.C.	Unpaired t test	6 mice H.C., 25 slices H.C.	< 0.0001
Fig2	B	Internal vs External T. w/. C.	Mann Whitney test	5 mice T. w/. C., 19 slices T. w/. C.	< 0.0001
Fig2	B	Internal vs External T. w/o. C.	Mann Whitney test	4 mice T. w/o. C., 13 slices T. w/o. C.	< 0.0001
Fig2	B	Lower blade vs Upper blade H.C.	Unpaired t test	6 mice H.C., 25 slices H.C.	< 0.0001
Fig2	B	Lower blade vs Upper blade T. w/. C.	Unpaired t test	5 mice T. w/. C., 19 slices T. w/. C.	< 0.0001
Fig2	B	Lower blade vs Upper blade T. w/o. C.	Mann Whitney test	4 mice T. w/o. C., 13 slices T. w/o. C.	< 0.0001
Fig3	B	Regression curve slope fosGFP$^+$ H.C. vs T. w/. C.	one-way ANOVA	15 mice H.C., 18 cells H.C., 7 mice T. w/. C., 16 cells T. w/. C.	< 0.0001

Fig3	B	Regression curve slope fosGFP^{+} T. w/. C. vs T. w/o. C.	one-way ANOVA	7 mice T. w/. C., 16 cells T. w/. C., 5 mice T. w/o. C., 17 cells T. w/o. C.	< 0.0001
Fig3	B	Regression curve slope fosGFP^{+} H.C. vs T. w/o. C.	one-way ANOVA	15 mice H.C., 18 cells H.C., 5 mice T. w/o. C., 17 cells T. w/o. C.	>0.05
Fig3	B	Regression curve slope fosGFP^{-} H.C. vs T. w/. C.	one-way ANOVA	17 mice H.C., 29 cells H.C., 11 mice T. w/. C., 26 cells T. w/. C.	>0.05
Fig3	B	Regression curve slope fosGFP^{-} T. w/. C. vs T. w/o. C.	one-way ANOVA	11 mice T. w/. C., 26 cells T. w/. C., 5 mice T. w/o. C., 8 cells T. w/o. C.	>0.05
Fig3	B	Regression curve slope fosGFP^{-} H.C. vs T. w/o. C.	one-way ANOVA	17 mice H.C., 29 cells H.C., 5 mice T. w/o. C., 8 cells T. w/o. C.	>0.05
Fig3	C	Gain fosGFP^{+} H.C. vs T. w/. C.	Unpaired t test	15 mice H.C., 18 cells H.C., 7 mice T. w/. C., 16 cells T. w/. C.	0.0076
Fig3	C	Gain fosGFP^{+} T. w/. C. vs T. w/o. C.	Unpaired t test	7 mice T. w/. C., 16 cells T. w/. C. 5 mice T. w/o. C., 17 cells T. w/o. C.	0.0238
Fig3	C	Gain fosGFP^{+} H.C. vs T. w/o. C.	Unpaired t test	15 mice H.C., 18 cells H.C., 5 mice T. w/o. C., 17 cells T. w/o. C.	0.5727
Fig3	C	Gain fosGFP^{-} H.C. vs T. w/. C.	Mann Whitney test	17 mice H.C., 29 cells H.C., 11 mice T. w/. C., 26 cells T. w/. C.	0.5780
Fig3	C	Gain fosGFP^{-} T. w/. C. vs T. w/o. C.	Unpaired t test	11 mice T. w/. C., 26 cells T. w/. C., 5 mice T. w/o. C., 8 cells T. w/o. C.	0.6227
Fig3	C	Gain fosGFP^{-} H.C. vs T. w/o. C.	Mann Whitney test	17 mice H.C., 29 cells H.C. 5 mice T. w/o. C., 8 cells T. w/o. C.	0.9516
Fig3	D	R input fosGFP^{+} H.C. vs T. w/. C.	Mann Whitney test	15 mice H.C., 21 cells H.C., 7 mice T. w/. C., 16 cells T. w/. C.	0.0132
Fig3	D	R input fosGFP^{+} T. w/. C. vs T. w/o. C.	Mann Whitney test	7 mice T. w/. C., 16 cells T. w/. C., 5 mice T. w/o. C., 20 cells T. w/o. C.	0.0240
Fig3	D	R input fosGFP^{+} H.C. vs T. w/o. C.	Unpaired t test	15 mice H.C., 21 cells H.C., 5 mice T. w/o. C., 20 cells T. w/o. C.	0.8415
Fig3	D	R input fosGFP^{-} H.C. vs T. w/. C.	Mann Whitney test	17 mice H.C., 29 cells H.C., 11 mice T. w/. C., 26 cells T. w/. C.	0.6820
Fig3	D	R input fosGFP^{-} T. w/. C. vs T. w/o. C.	Unpaired t test	11 mice T. w/. C., 26 cells T. w/. C., 5 mice T. w/o. C., 8 cells T. w/o. C.	0.5478
Fig3	D	R input fosGFP^{-} H.C. vs T. w/o. C.	Mann Whitney test	17 mice H.C., 29 cells H.C., 5 mice T. w/o. C., 8 cells T. w/o. C.	0.6250

Fig3	E	Rheobase fosGFP^{+} H.C. vs T. w/. C.	Mann Whitney test	15 mice H.C., 21 cells H.C. , 7 mice T. w/. C., 16 cells T. w/. C.	0.0029
Fig3	E	Rheobase fosGFP^{+} T. w/. C. vs T. w/o. C.	Mann Whitney test	7 mice T. w/. C., 16 cells T. w/. C., 5 mice T. w/o. C., 20 cells T. w/o. C.	0.0128
Fig3	E	Rheobase fosGFP^{+} H.C. vs T. w/o. C.	Mann Whitney test	15 mice H.C., 21 cells H.C., 5 mice T. w/o. C., 20 cells T. w/o. C.	0.4253
Fig3	E	Rheobase fosGFP^{-} H.C. vs T. w/. C	Mann Whitney test	17 mice H.C., 29 cells H.C., 11 mice T. w/. C., 26 cells T. w/. C.	0.2106
Fig3	E	Rheobase fosGFP^{-} T. w/. C. vs T. w/o. C.	Mann Whitney test	11 mice T. w/. C., 26 cells T. w/. C., 5 mice T. w/o. C., 8 cells T. w/o. C.	0.6437
Fig3	E	Rheobase fosGFP^{-} H.C. vs T. w/o. C.	Mann Whitney test	17 mice H.C., 29 cells H.C., 5 mice T. w/o. C., 8 cells T. w/o. C.	0.1664
Fig4	B	fosGFP^{+} distribution Phase plot 1peak vs 2peaks	χ^2 test	15 mice H.C., 7 mice T. w/. C., 5 mice T. w/o C., 56 cells	0.9563
Fig4	B	fosGFP^{-} distribution Phase plot 1peak vs 2peaks	χ^2 test	11 mice H.C., 17 mice T. w/. C., 5 mice T. w/o C., 63 cells	0.9468
Fig4	B	fosGFP^{+} vs fosGFP^{-} distribution Phase plot 1peak vs 2peaks	Fisher's exact test	48 mice, 56 fosGFP^{+} cells, 63 fosGFP^{-} cells	0.0002
Fig5	C	AIS length fosGFP^{+} vs fosGFP^{-} H.C.	Unpaired t test	5 mice H.C., 47 fosGFP^{+} cells, 47 fosGFP^{-} cells	< 0.0001
Fig5	C	AIS length fosGFP^{+} vs fosGFP^{-} T. w/. C.	Unpaired t test	5 mice T. w/. C., 57 fosGFP^{+} cells, 57 fosGFP^{-} cells	< 0.0001
Fig5	C	AIS length fosGFP^{+} vs fosGFP^{-} T. w/o. C.	Unpaired t test	5 mice T. w/o. C. 38 fosGFP^{+} cells, 34 fosGFP^{-} cells	< 0.0001
Fig5	C	AIS distance from the soma fosGFP^{-} vs fosGFP^{+} H.C.	Mann Whitney test	5 mice H.C., 47 fosGFP^{+} cells, 47 fosGFP^{-} cells	0.1186
Fig5	C	AIS distance from the soma fosGFP^{-} vs fosGFP^{+} T. w/. C.	Mann Whitney test	5 mice T. w/. C., 57 fosGFP^{+} cells, 57 fosGFP^{-} cells	0.1275
Fig5	C	AIS distance from the soma fosGFP^{-} vs fosGFP^{+} T. w/o. C.	Unpaired t test	5 mice T. w/o. C. 38 fosGFP^{+} cells, 34 fosGFP^{-} cells	0.3736

FigS2	B	AIS normalized radial position fosGFP^{-} vs fosGFP^{+} H.C.	Mann Whitney test	5 mice H.C., 47 fosGFP^{+} cells, 47 fosGFP^{-} cells	0.9534
FigS2	B	AIS normalized radial position fosGFP^{-} vs fosGFP^{+} T. w/. C.	Mann Whitney test	5 mice T. w/. C., 57 fosGFP^{+} cells, 57 fosGFP^{-} cells	0.3753
FigS2	B	AIS normalized radial position fosGFP^{-} vs fosGFP^{+} T. w/o. C.	Mann Whitney test	5 mice T. w/o. C., 38 fosGFP^{+} cells, 34 fosGFP^{-} cells	0.4802

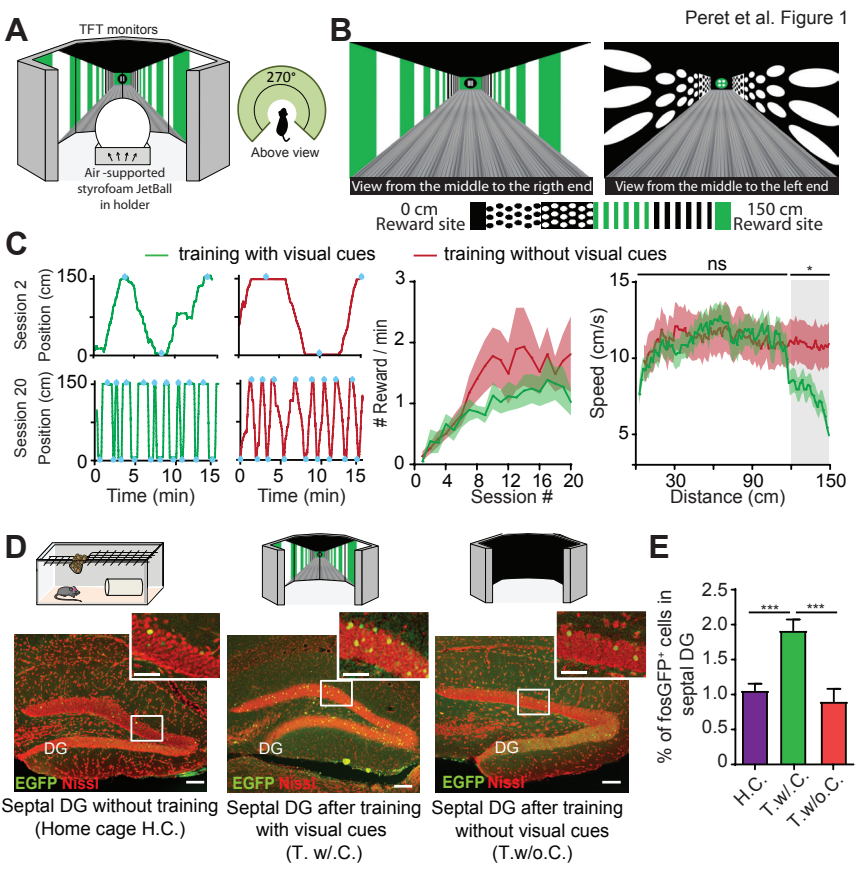

Figure 1. Increased number in fosGFP⁺ neurons in mice trained with visual cues.
(A) Schematic representation of the experimental set-up. Mice were fixed to an arm with a screw through a chronically implanted head-bar. By moving an air-flow-supported styrofoam JetBall, mice were navigating in a virtual environment provided through six TFT monitors surrounding the JetBall (270°). Reward was delivered to the animal through a plastic tube.
(B) Screenshots from the middle to the right and left ends of the track. The track (150 cm) was divided into four regions with different textures (black dots, white dots, vertical green stripes and vertical black stripes). Water rewards were given at the ends of the track, with available rewards alternating between reward sites.
(C) Sample trajectories for an individual mouse on training sessions 2 and 20; position is the animal's location along the 150 cm-long linear track axis and blue dots indicate rewards (left panel). Rate of rewards vs. session numbers for mice trained with (green) or without (red) visual cues (middle panel). Running speed of mice as a function of the position on the linear track for mice trained with (green) or without (red) visual cues (right panel). Grey box represent the deceleration zone (from 120 to 150 cm).
(D) On the top, schematic of the three different experimental conditions: home cage, training in VR with or without visual cues. On the bottom: Nissl staining (red) of septal DG with an immunostaining using anti-EGFP antibody (green); scale bar 100 µm. Insets show parts of septal DG at higher magnification; scale bar 50 µm.
(E) Bar graphs displaying the percentage of fosGFP⁺ cells activated in septal DG in mice in home cage (H.C.), mice trained with (T.w/.C.) or without (T.w/o.C.) visual cues.
Data are shown as mean ± SEM. *$p<0.05$,***$p<0.0001$, ns, $p>0.05$. In this and following figures the statistics are shown in the supplementary table.

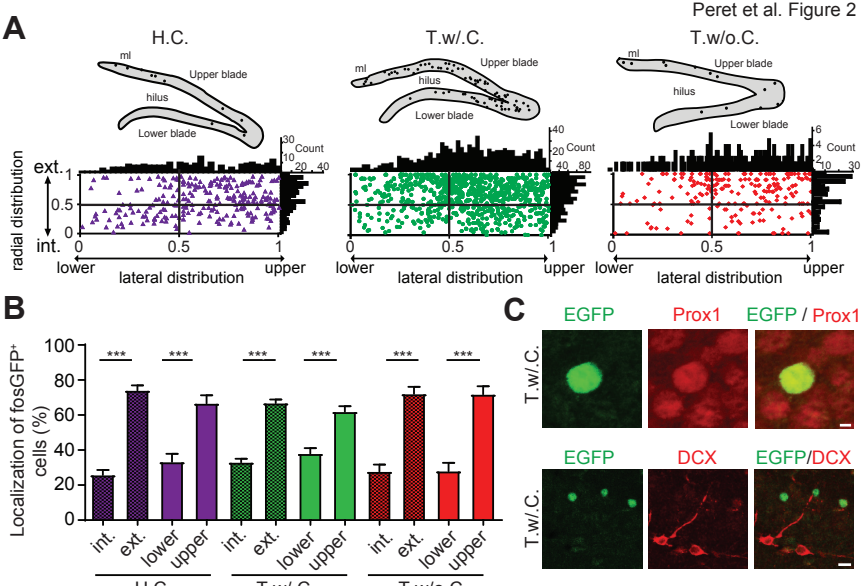

Figure 2. fosGFP⁺ cells display characteristics of mature DGCs.

(A) Top: Schematic illustration of DG from confocal image of figure 1D with fosGFP⁺ cells represented as solid circles. Bottom: Plot diagram representing lateral and radial distributions of fosGFP⁺ from septal DG in mice in home cage (H.C., triangles), trained with (T.w/.C., circles) or without (T.w/o.C., diamonds) visual cues. The tip of lower blade of granule cell layer is defined as 0 and that of upper blade as 1 in the lateral direction. The border between granule cell layer and the hilus is defined as 0 (int. for internal) and that between granule cell layer and molecular layer (ml) as 1 (ext. for external) in the radial direction. The histograms above and on the right of the square diagram indicate the number of fosGFP⁺ cells in the lateral and radial direction, respectively.

(B) Bar graph of the percentage of localization of fosGFP⁺ cells for radial (int. vs ext.) and lateral (lower vs upper) distributions in H.C., T.w/.C. and T.w/o.C. conditions. Data are shown as mean ± SEM. ***$p<0.0001$.

(C) Top: Representative double immunostaining using anti-EGFP antibody associated with anti-Prox1. Bottom: Representative double immunostaining using anti-EGFP antibody associated with anti-DCX; scale bar 10 µm.

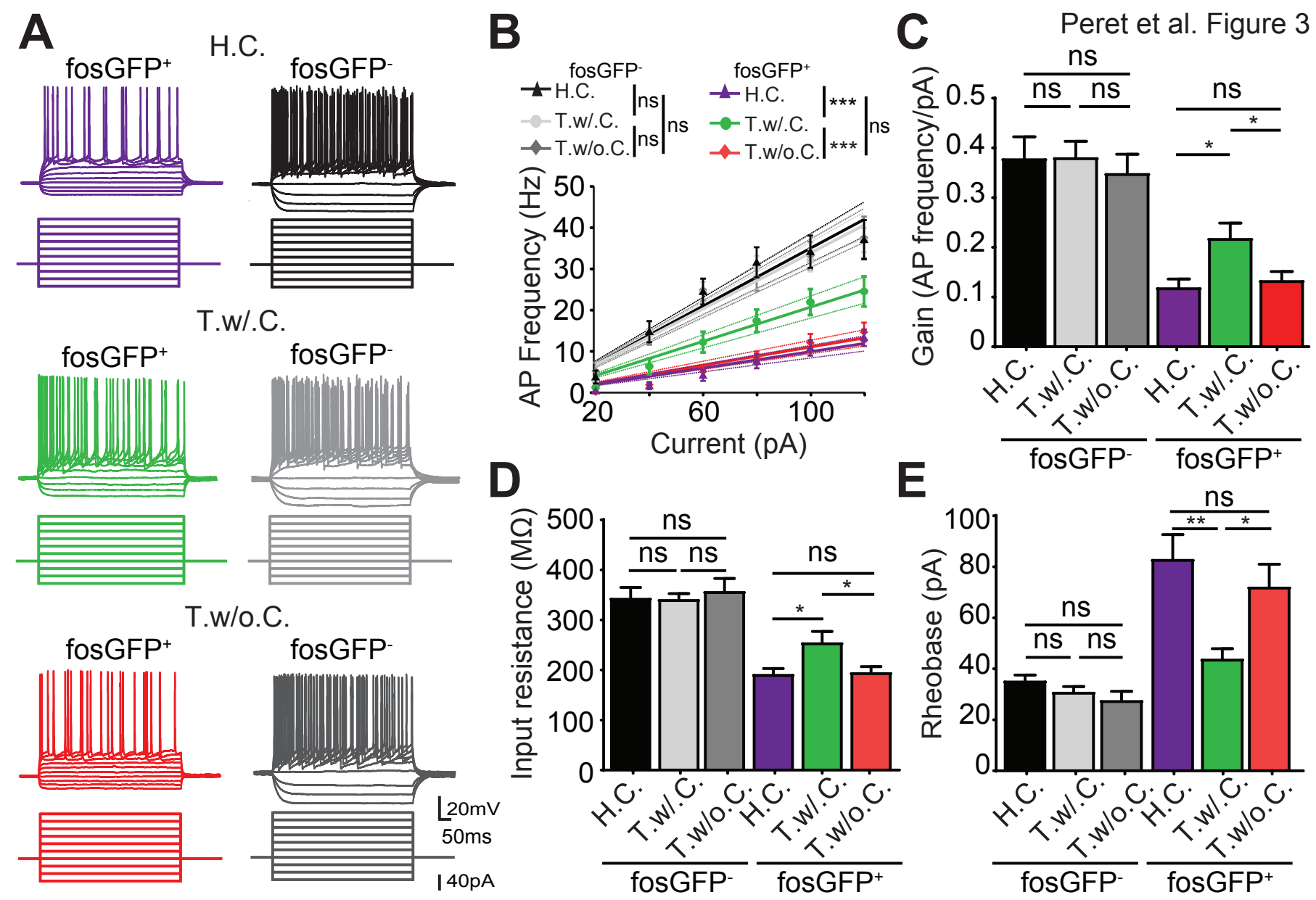

Figure 3. fosGFP⁺ DGCs display different intrinsic properties.
(A) Representative membrane potential variation and action potential discharges evoked in fosGFP⁻ or fosGFP⁺ DGCs in mice in home cage (H.C.) (top), trained with (T.w/.C.) (middle) or without (bottom) visual cues (T.w/o.C.) evoked by 500 ms current steps varying from -60 pA to +120 pA by 20 pA step increments, at a holding potential of -60 mV.
(B) Linear regression curves (solid lines, dashed lines are for error interval) fitted for the mean discharge frequency/injected current relationship (symbols) of fosGFP⁻ and fosGFP⁺ DGCs in H.C. (triangle), T.w/.C. (square) and T.w/o.C. (diamond) conditions.
(C) Bar graphs displaying the firing gain, (D) the input resistance, and (E) rheobase of fosGFP⁻ and fosGFP⁺ DGCs in each condition. Note that the f/I plots, the gain, the input resistance, and the rheobase are significantly different when comparing fosGFP⁻ with fosGFP⁺ and when comparing fosGFP⁺ in H.C. with fosGFP⁺ in T.w/.C. conditions. Data are shown as mean ± SEM. *p<0.05,**p<0.01,***p<0.0001, ns p>0.05.

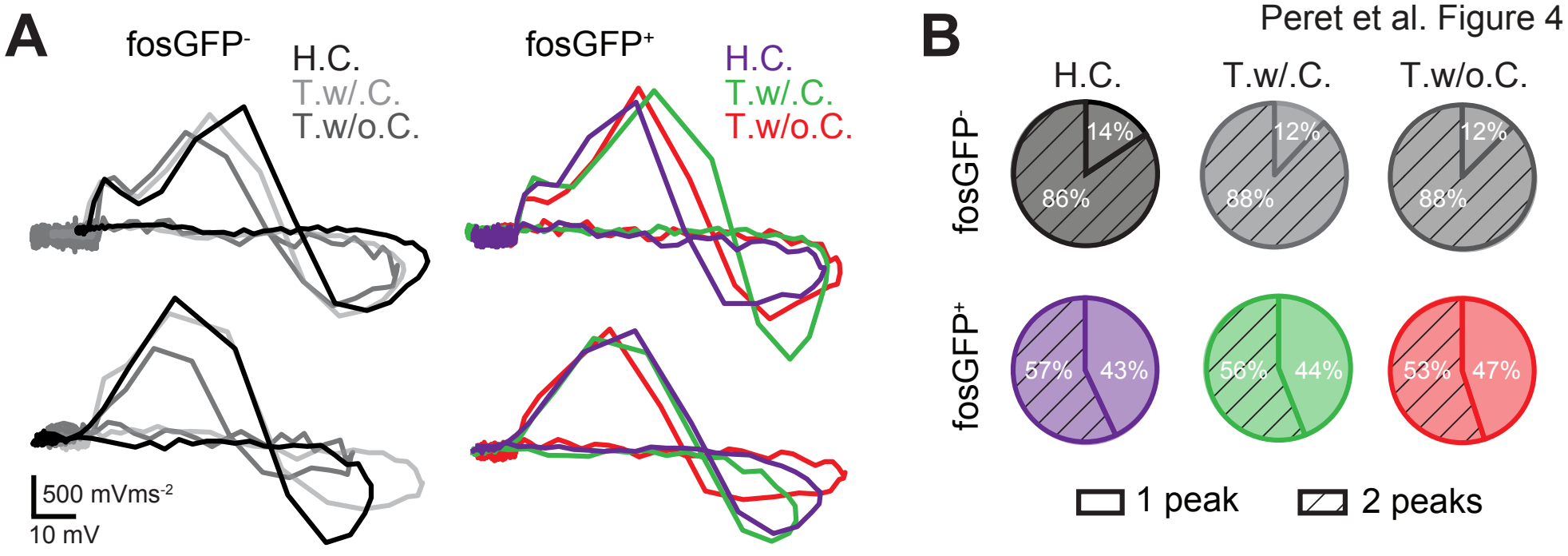

Figure 4. fosGFP$^+$ DGCs display a modified AP waveform.
(A) Representative superimposed phase plots of the 2nd derivative of the somatic membrane potential (d^2V/dt^2) vs. membrane potential (Vm) of action potentials recorded in fosGFP$^-$ and fosGFP$^+$ DGCs in mice in home cage (H.C.), trained with (T.w/.C.) or without (T.w/o.C.) visual cues; threshold has been taken as reference. Top: phase plots of action potential with two peaks (the first one reflecting the spike initiation in AIS and the second one the somato-dendritic spike). Bottom: phase plots of action potential showing only one peak, the somato-dendritic component.
(B) Pie charts of distribution of phase plots with 1 (plain area) or 2 (striped area) peaks in fosGFP$^-$ and fosGFP$^+$ DGCs in each condition. Note that about 90% of fosGFP$^-$ DGCs display two peaks, whereas about 50% of fosGFP$^+$ DGCs display only one peak.

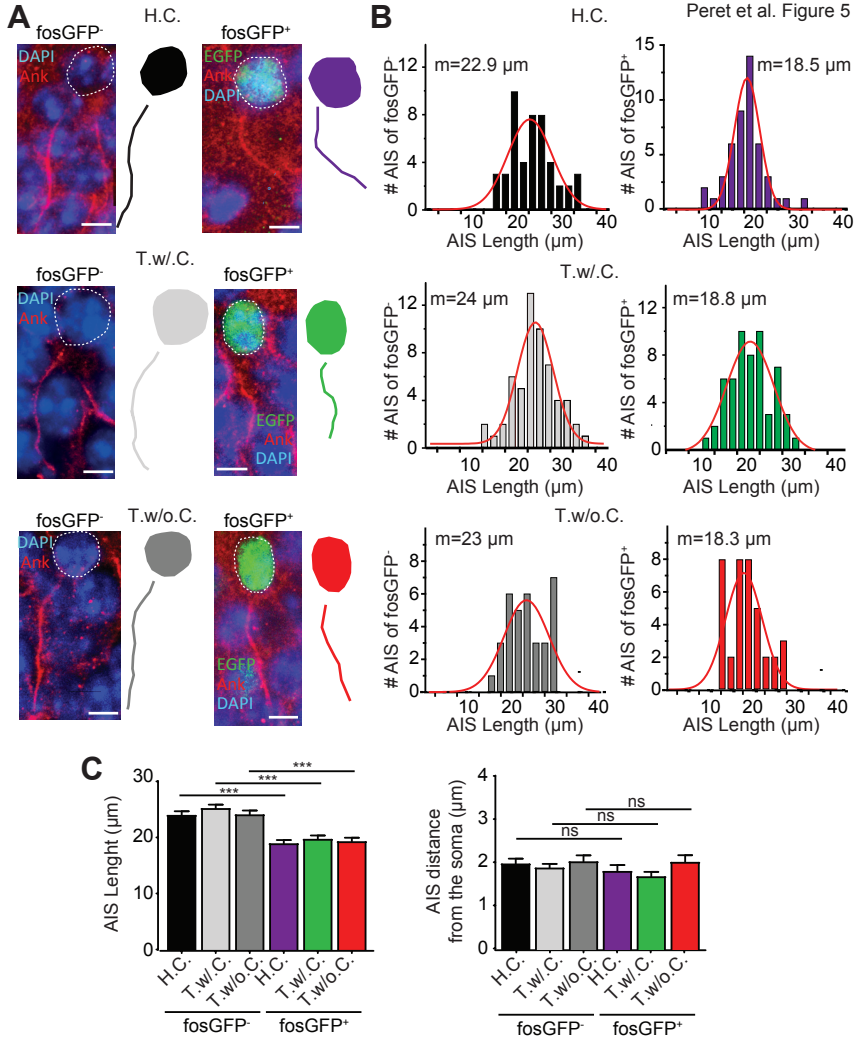

Figure 5. fosGFP⁺ DGCs display a shorter AIS length.

(A) Projection of confocal images of fosGFP⁻ (left) and fosGFP⁺ (right) showing immunostaining using anti-EGFP, anti-Ankyrin-G antibodies and DAPI and their Neurolucida reconstructions in mice in home cage (H.C., top), trained with (T.w/.C., middle) or without (T.w/o.C., bottom) visual cues ; scale bar, 5 µm.

(B) AIS length distribution of fosGFP⁻ (left) or fosGFP⁺ (right) in H.C. (top), T.w/.C. (middle) and T.w/o.C. (bottom) conditions; m indicates the value of the median of the Gaussian fit. Note the shift of AIS length distribution towards smaller values when comparing fosGFP⁺ to fosGFP⁻ cells.

(C) Bar graphs displaying the AIS length (left) and the distance from the soma (right) of fosGFP⁻ and fosGFP⁺ in H.C., T.w/.C. and T.w/o.C. conditions. Note that the length of AIS is significantly shorter in fosGFP⁺ DGCs. Data are shown as mean ± SEM. ***p<0.0001, ns, p>0.05.

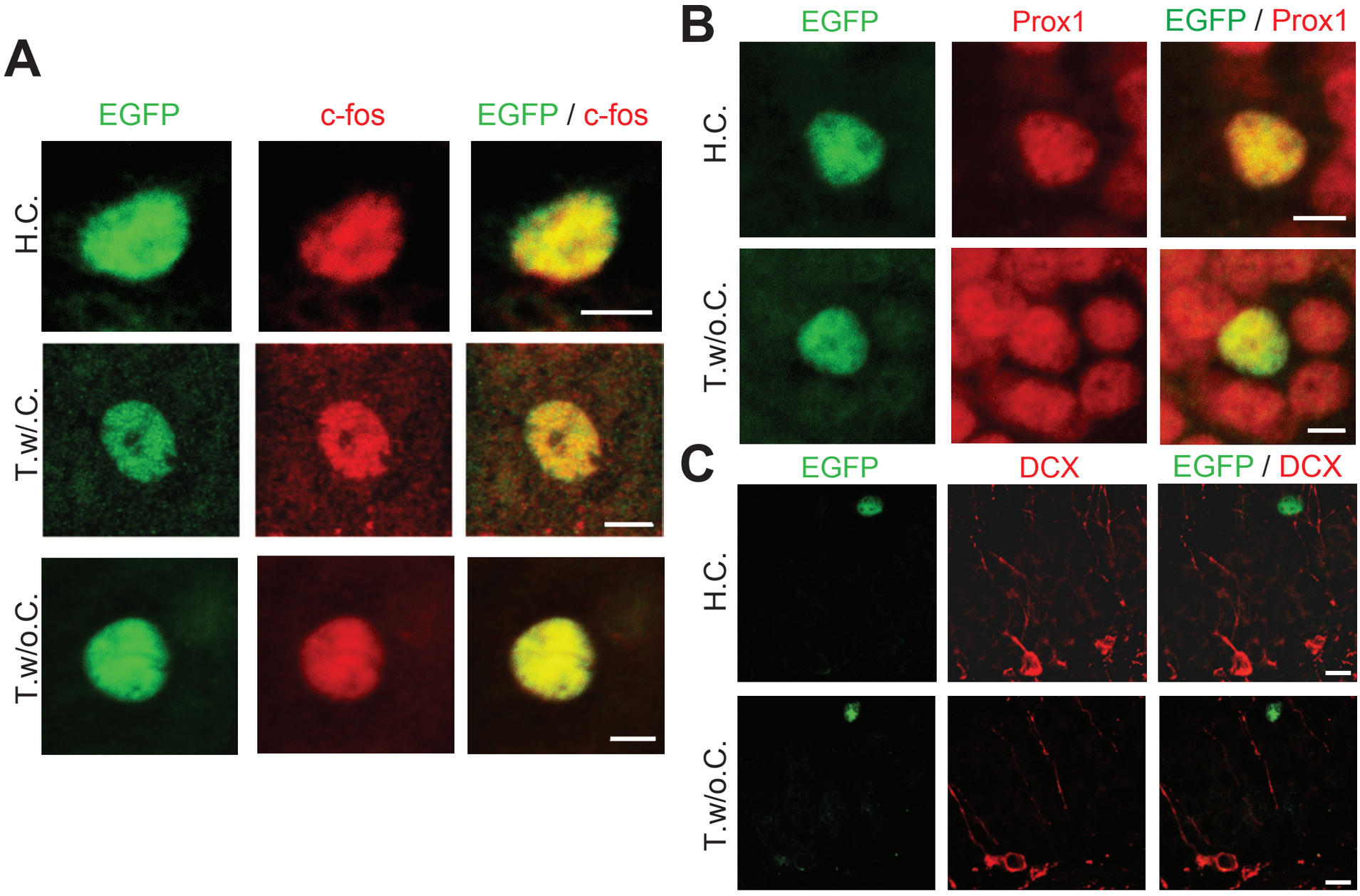

Supplementary figure 1.

(A) Representative double immunostaining using anti-EGFP antibody associated with anti-c-fos in mice in home cage (H.C), trained with (T.w/.C.) or without (T.w/o.C.) visual cues; scale bar 10 µm.

(B) Representative double immunostaining using anti-EGFP antibody associated with anti-Prox1 in each condition; scale bar 10 µm.

(C) Representative double immunostaining using anti-EGFP antibody associated with anti-DCX in each condition; scale bar 10 µm.

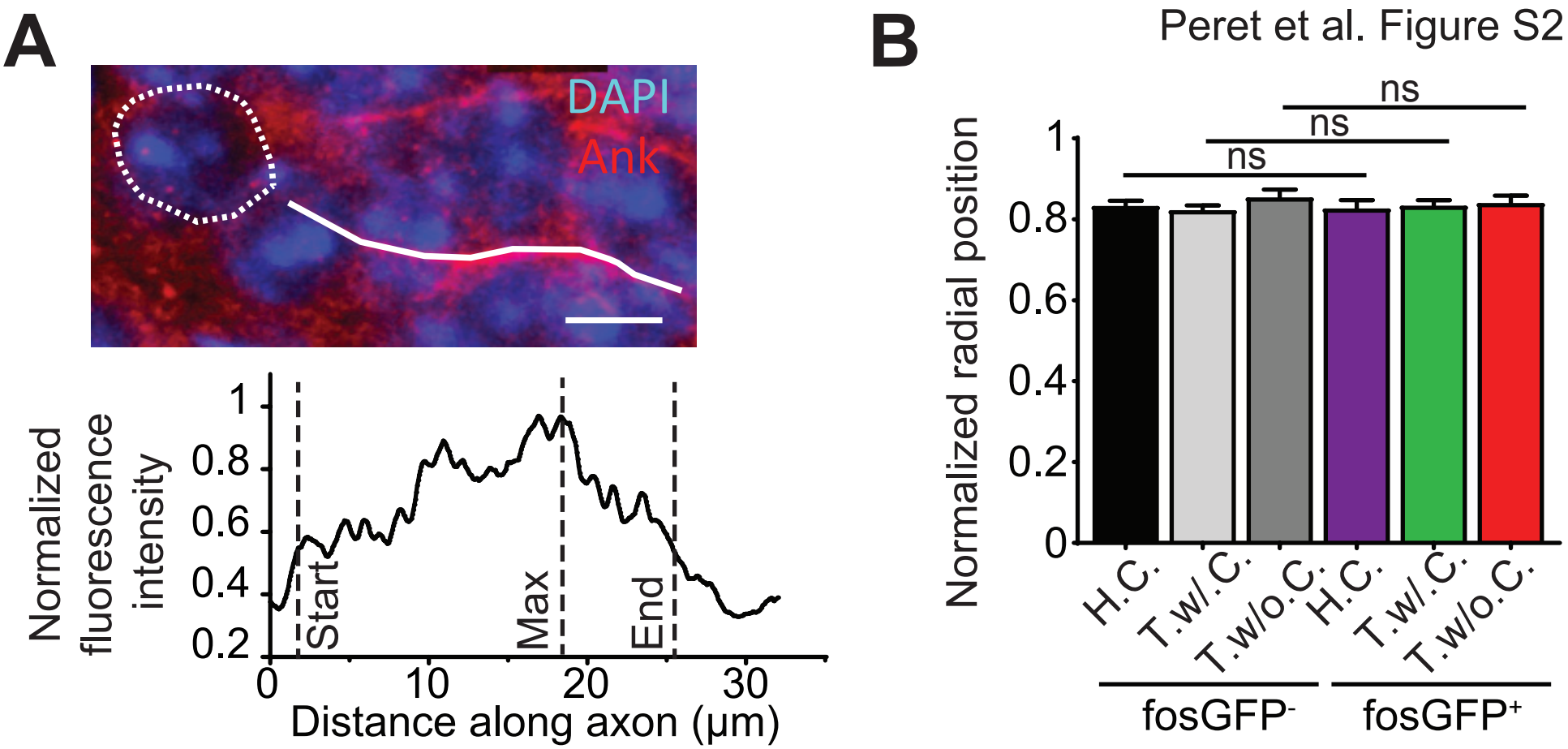

Supplementary figure 2.

(A) Top, projection of a confocal image showing immunostaining using anti-Ankyrin-G antibodies and DAPI and the superimposed Neurolucida reconstructions of the soma (dotted lines) and axon initial segment (solid line); scale bar, 5 µm. Bottom, fluorescence intensity along the axon initial segment.

(B) Bar graphs displaying the normalized radial position of fosGFP$^-$ and fosGFP$^+$ cells used to analyse AIS length and AIS location from the soma in mice in home cage (H.C.), trained with (T.w/.C.) or without (T.w/o.C.) visual cues. Data are shown as mean ± SEM. ns $p>0.05$.